Experimental and numerical research on a novel hysteretic dissipative and easily repairable device for composite steel-concrete frame structures

Diogo Jorge Santos Cabrita

Department of Civil Engineering, Architecture and Georesources of Instituto Superior Técnico, December 2020

Abstract: In the structural design research and professional activities, there is an increasing requirement of safety and structure resilience when it comes to seismic events. Taking the experience collected in previous researches, a novel dissipative and repairable bracing device connection was developed. The device is applied in composite steel-concrete frame structures and comprises a transversal steel pin that dissipates energy through yielding. In order to access the local performance of the device, experimental and numerical studies on eight different configurations are investigated. The study encompasses two pin geometries, chamfered or circular with different weld configurations and an innovative feature, the guiding plates. The device showed a good hysteretic behaviour and good dissipation energy capacity. The damage was concentrated on the dissipative element, the pin. The eye-bar plates suffered yielding and ovalization. Results showed a ductile failure due to bending for chamfered pin sections and a generally shear induced failure for welded circular pin sections. The bending of the eye-bar plates observed in previous research was successfully eliminated due to the implementation of spacers. Lateral displacements were significantly reduced due to the implementation of the guiding plates. Numerical models were developed for a more in-depth evaluation of the bracing connection performance. Combined hardening was introduced to simulate the cyclic behaviour of the steel material and ductile material was introduced to simulate the failure of the pin. The simulations corroborated the promising results of the experimental tests. Python scripts were developed to automate some steps of the numerical modeling and postprocessing.

Keywords: Bracing connection, repairable dissipative devices, cyclic experimental tests, hysteretic behaviour, numerical modelling, ductile damage.

1. Introduction

Under seismic action, structures are submitted to imposed displacements. Consequently, high forces are originated that produce permanent deformations, local buckling and collapse of essential structural elements. These damages may lead to stability problems, structural collapse, loss of lives and economic drops. The dissipative devices offer advantageous seismic protection to structures. Hysteretic devices are amongst the most efficient and economical dissipative devices. The hysteretic devices aim

to make use of the formation of plastic hinges to dissipate energy.

2. Experimental Studies

The aim of this study was to compare and evaluate the performance of eight previously defined configurations, presented in Table 1, of the innovative Dissipative and Repairable Bracing Connection (DRBrC) device. In an effort to assess the influence of different variables that define the configurations tested. The experimental test process consists of imposing uniaxial displacements following the ECCS protocol (ECCS, 1986) through a mechanical actuator, on a brace equipped with the dissipative device. An installed load cell then measures the force that the pin-device is subjected. A scheme of the experimental setup is presented in Figure 3.

2.1. DRBrC Specimen

Previous research programs (Plumier et al., 2004) led to the current design of the device presented in Figure 1. In the DRBrC device a pin, the dissipative element, is subjected to four-point bending which behaves in a relatively simple and predictable way, resembling a beam. The energy dissipation is thus obtained by accumulation of permanent plastic deformations in the pin.

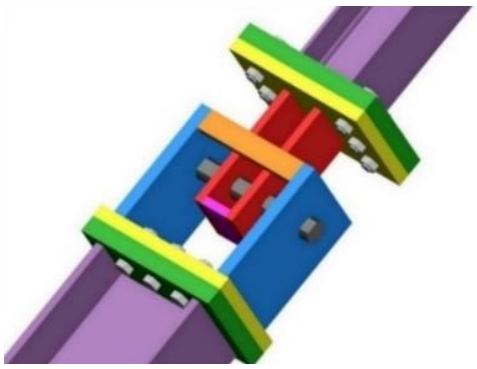

Figure 1: DRBrC device overall view.

The DRBrC dissipative device is meant to be applied in steel or combined steel-concrete concentrically braced frames that allow for slight accommodation of imposed displacements.

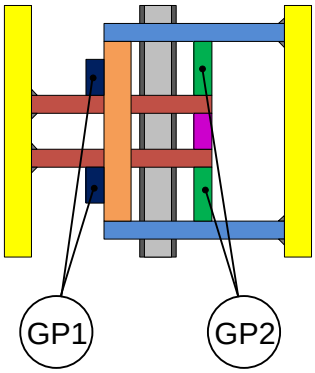

Figure 2: Guiding plates

The experimental studies encompass two types of pin section geometry, chamfered pin section (R) and circular pin section (C) configurations. In the case of the circular pin specimens, in order to test different pin fixing solutions to the external eye-bar plate, three weld configurations were considered. In W1 a pair of exterior welds were applied. In W2 a pair of exterior and a pair of interior welds were applied. In W3 only one exterior weld was applied, allowing the pin to freely rotate and extend on the other extremity. Additionally, the application of guiding plates, presented in Figure 2 were investigated.

Table 1: Tested specimens

Acronym	Pin		Guiding plates	
	$\Phi\ (mm)$	Material	GP1	GP2
01R	50	SOFMAN		
02R	50	IST	X	
03R	50	IST	X	
04R	50	IST	X	X
15C	50 W1	SOFMAN	X	
16C	50 W2	IST	X	X
17C	50 W1	IST	X	X
18C	50 W3	IST	X	X

.

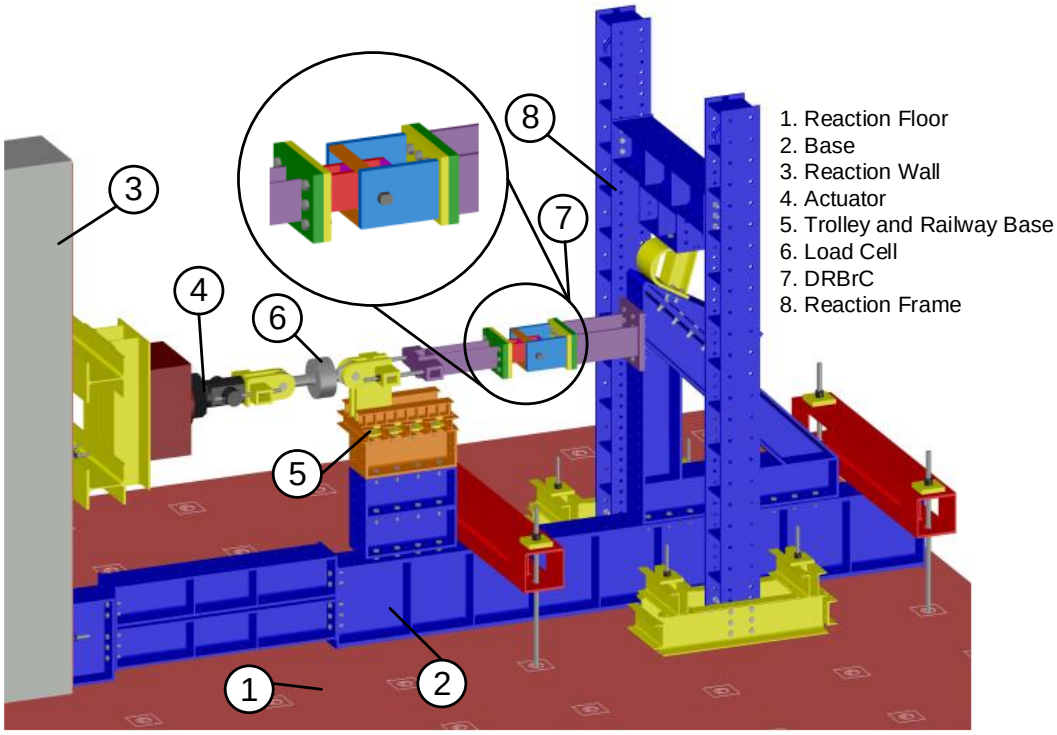

Figure 3: Fixed equipment scheme.

3. Analysis of the Experimental Results

Due to the bearing at the pin-plates interface caused by the ovalization of the eye-bar plates, the force-displacement curves presented considerable pinching. Pinching results in energy loss and was an issue addressed in the previous researches (Vayas et al., 2017), On a positive note, an evident improvement was the elimination of the transverse bending of the eye-bar plates due to the inclusion of spacer elements. Regarding the pin section geometry, all chamfered sections presented a failure mode due to bending, in the mid-section of the pin, as it is ideal. On the other hand, the circular sections with weld configurations presented a failure mode due to shear. Because the chamfered pin sections can elongate freely out-of-plane, the middle section presented an advanced section reduction. This leads to the development of the local plastic hinge at this point, and consequently to the failure through accumulation of plasticity. On the other hand, since the circular sections configurations have welds that prevent the pin from elongation, the pin section is barely reduced. Thus, the circular welded section pins suffered a brittle failure in the areas of contact with the eye-bar plates. It is possible to conclude that the elongation of the pin plays a fundamental role on the failure mode and cyclic behaviour of the specimens. Additionally, two groups of guiding plates were investigated. When both guiding plate groups were applied the results showed a pronounced and symmetrical reduction on the lateral displacement of the external eye-bar plates. The best results were obtained when both groups of guiding plates are applied considering that the maximum lateral displacements, represented in Figure 4, were reduced from $15\,mm$ to $3\,mm$. Energy dissipation was determined from the force-displacement curves. The total dissipated

energy and the number of cycles for the chamfered pin section test specimens is presented in Table 2.

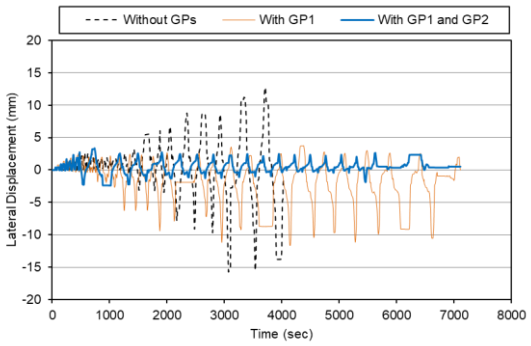

Figure 4: Guiding plates influence on lateral displacement.

In the case of the chamfered sections test, the test specimen 02R showed the highest energy dissipated value, while test specimen 03R resulted in the lowest dissipated energy.

Table 2: Total dissipated energy and nr. of cycles obtained in chamfered pin section tests.

Test Nr.	01R	02R	03R	04R
Dissipated Energy (kNm)	110	200	**208**	190
Nr of Cycles	19	29	23	**35**

Similarly, the total dissipated energy and the number of cycles for the circular pin section test specimens is presented in Table 3. In this case, the test specimen 17C presented the highest dissipated energy and the highest number of cycles performed, while the test specimen 16C presented the lowest value of dissipated energy. All test specimens reached pin total pin failure except test specimen 01R and 15C due to the high resistance of the pin material used. This material was subsequently replaced for the remaining test specimens that reached pin failure.

Table 3: Total dissipated energy and nr. of cycles obtained in circular pin section tests.

Test Nr.	15C	16C	17C	18C
Dissipated Energy (kNm)	224	97	**452**	340
Nr of Cycles	27	29	**57**	33

4. Numerical models

4.1. Finite element model

All the experimental tests, eight in total, were simulated using the general-purpose software ABAQUS/Standard. This software has Python embedded, which allowed the development of scripts to automate procedures of the modelling and the postprocessing.

The different characteristics between the tested configurations such as pin material, pin section geometry, load histories and weld positions, in the case of circular sections, were all taken into consideration in the finite element models. The chamfered pin section tests have a completely symmetrical design in two planes, whereas the weld configurations applied in the circular pin are not always symmetrical. Therefore, the chamfered pin section tests were modelled taking advantage of the symmetry, whereas the circular pin section tests and the simulations present a complete model.

Regarding material properties the elastic behaviour is considered to be isotropic and it is defined by the Young's modulus and Poisson's ratio. The conventional carbon steel mechanical properties were assumed, namely the Young's modulus of 210GPa and Poisson's ratio of 0.3.

The steel materials involved can be classified as ductile materials given that they present large inelastic strains at orders of magnitude less that the Young's modulus. The input stress-strain values introduced in finite-element models were the true stress and true strain

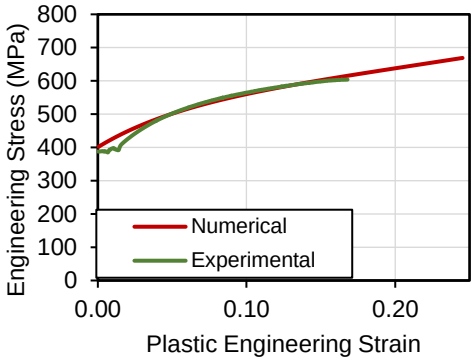

(a)

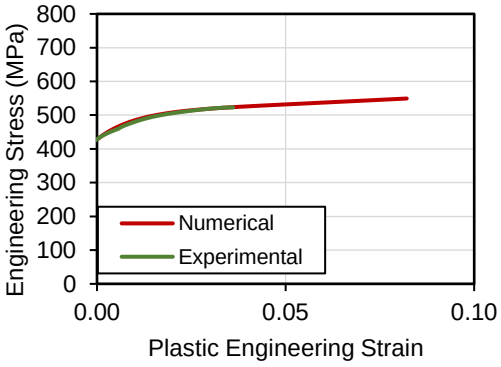

(b)

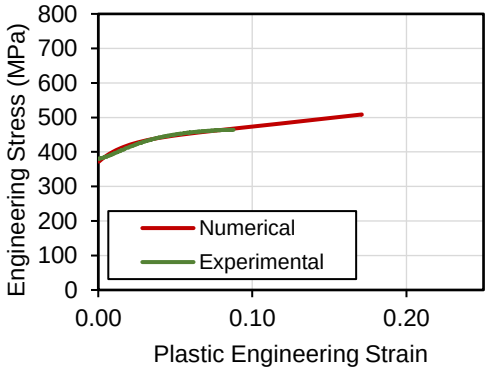

(c)

Figure 5: Combined hardening calibration: (a) SOFMAN plate material, (b) SOFMAN pin material and (c) IST pin material.

Table 4: Combined hardening parameters.

Element	$\sigma^0, \sigma\|_0$ (MPa)	C	γ	Q_∞	b
Plates SOFMAN Pin	400	2200	18	0	0
	420	8000	100	0	0
IST Pin	380	3400	58	0	0

The plastic hardening modelling for cyclic steel elements was made considering the combined hardening theory present in ABAQUS. This theory is based on the formulations developed by Armstrong-Frederick and Chaboche. The combined hardening parameters were derived preliminary in a curve fitting process, where the expressions of the calibration method adopted (Myers et al., 2009 - Appendix D), were applied. Then, the tensile tests were modelled, and, through a process of a trial and error and curve fitting, Figure 5, the combined hardening parameters were adjusted. Thus, the calibrated parameters for each element of the device applied in the numerical models are presented in Table 4.

4.2. Numerical results

The resulting equivalent plastic strain $PEEQ$ obtained for a chamfered pin and a circular pin model at an advanced cycle is represented in Figure 7. This value is taken as a qualitative evidence of the inelastic deformation. If this variable is greater than zero, the material has yielded. The pin element has reached yielding stresses for almost all its geometry.

The eye-bar plates reached the plastic range in the proximity of the pin contact. In the case of the

circular section tests the welds reached full plasticity. The remaining elements remain in the elastic range.

Additionally, normal stresses σ_{33} were requested to access the symmetrical behaviour and to compare the dimensions of stresses developed between the chamfered pin section and the circular pin section models. The Figure 8 shows a clear symmetry in the normal stresses. Comparing both pin section configurations results it is possible to observe that the circular pin configuration developed higher values of normal stresses than the chamfered pin configuration. Additionally, the area affected with these stresses is broader in the circular pin configuration.

5. Numerical-Experimental Comparison

The validation of the numerical models consists of verifying that the numerical models faithfully simulate the observed experimental behaviour of the device. In order to do this the numerical and experimental force-displacement curves, envelope curves, excursion diagrams, peak force diagrams, and dissipated energy diagrams were analysed.

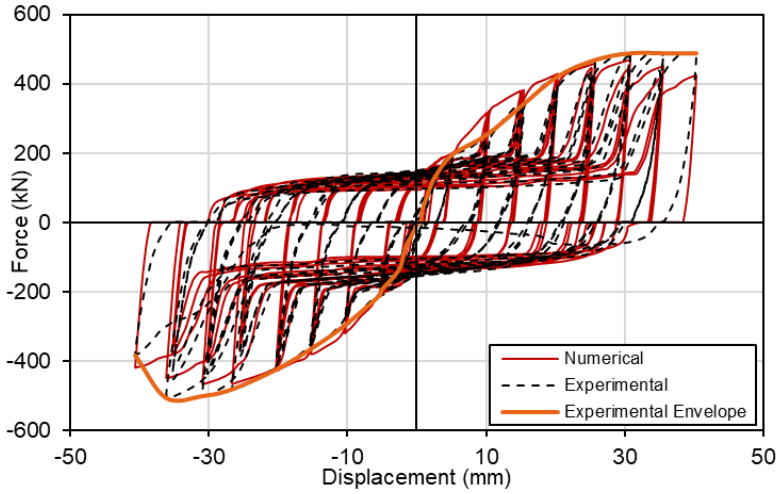

Figure 6: Force-displacement curve comparison of a chamfered pin configuration.

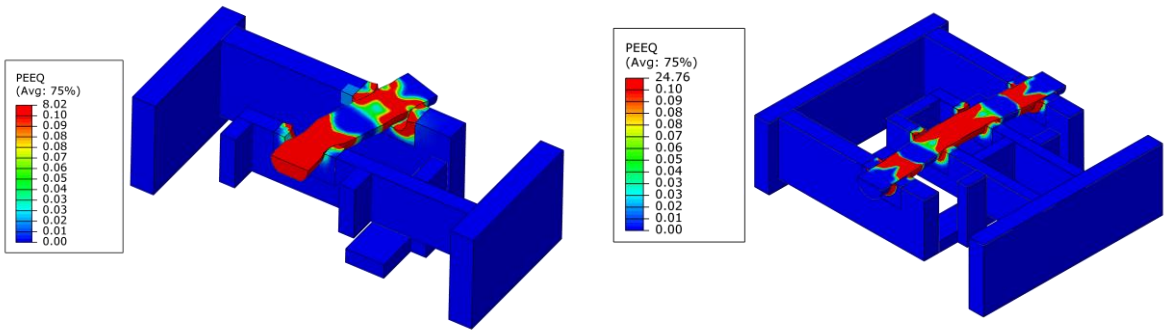

(a) (b)

Figure 7: Equivalent plastic strains $PEEQ$: (a) chamfered section, (b) circular section.

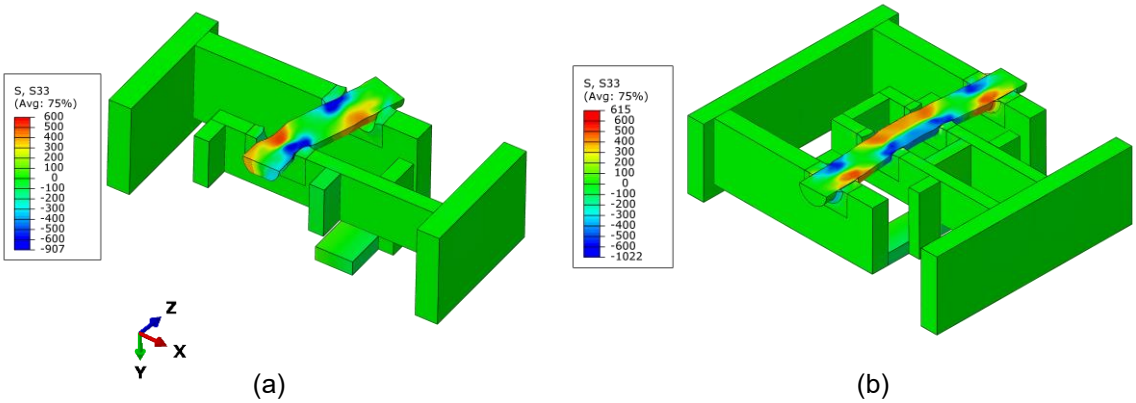

(a) (b)

Figure 8: Normal stresses σ_{33}: (a) chamfered section, (b) circular section.

The numerical force-displacement curves obtained in the case of the chamfered pin configurations, Figure 6, did not show the gradual stiffness degradation in the unloading phases and presented a more pronounced yielding softening at the advanced cycles when comparing to the experimental results. Nevertheless, the resulting maximum force as well as the plateaus of the numerical force-displacement curves show an excellent correspondence to the experimental force-displacement curves. However, circular pin section numerical models showed a significant deviation from the experimental tests results. Mainly because of the welded sections, which the interactions are intricate to simulate, and thus make the finite-element models of these configurations more complex.

The numerical model of the circular pin section configurations failed to simulate the pronounced pinching effect, the yielding softening, and the stiffness degradation on both loading and unloading phases of the hysteresis loop. This is because the welds were damaged progressively and reached failure soon in the experimental test, an occurrence that the numerical models do not consider. For that reason and in order to attain failure in the numerical models, damage criteria was investigated and applied. The Figure 10 presents the force-displacement curves for a circular pin section numerical model without and with implemented damage. This failure mechanism manifests itself in the softening of the yield stress and degradation of the elastic stiffness.

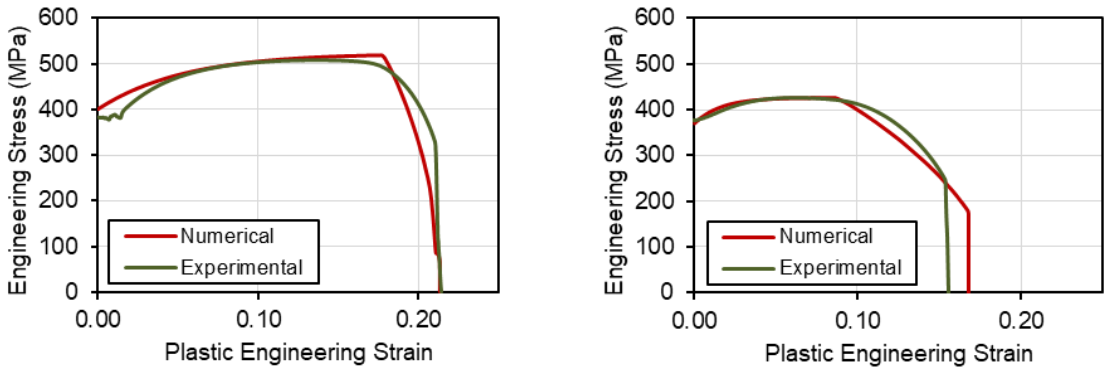

(a) (b)

Figure 9: Damage criteria calibration: (a) plate elements, (b) pin element.

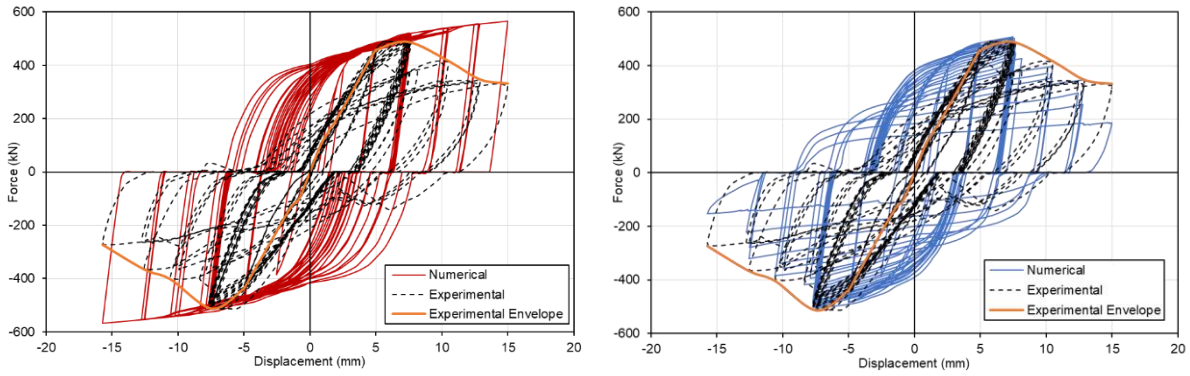

(a) (b)

Figure 10: Force-displacement curves comparison for a circular pin configuration: (a) no damage, (b) with damage implemented.

Ductile damage is defined through a damage initiation criterion and a damage evolution law (ABAQUS, 2012). The damage initiation criterion is defined by the fracture strain value, that corresponds to the equivalent true plastic strain at the onset of damage, $\bar{\varepsilon}_0^{pl}$.

The damage evolution is defined in terms of fracture energy G_f. This parameter was determined considering the force-displacement curve obtained experimentally and the equivalent length of the numerical model elements. Thus, applying the expression:

$$Gf = \int_0^{\bar{u}_f^{pl}} \frac{F}{L^2} d\bar{u}^{pl} \qquad (1)$$

The damage criteria was only applied in the pin element and in the welds, since these are the only elements that are subjected to failure conditions.

To determine the damage parameters, a process identical to the calibration of the combined plastic hardening, the simulation of the tensile tests, was performed. Through trial and error, the analytically determined parameters were afterwards adjusted by a curve fitting process considering the engineering stress-strain curves obtained experimentally. The resulting curves of this calibration process are presented in presented in Figure 9. Additionally, the calibrated damage parameters are presented in Table 5.

The numerical model with implemented damage showed the clear softening of the yield stress with the increasing of the imposed displacements.

Table 5: Damage parameters.

Element	Fracture Strain	Fracture Energy (N/mm)
Pin	0.11	6800
Plate/Weld	0.22	6800

Additionally, although the stiffness degradation cannot be clearly observed in the numerical force-displacement curve, it was verified analytically. Therefore, it was confirmed that the rate of the softening of the yield stress was equivalent to the rate of stiffness degradation, and thus related to the damage parameter. For that reason, the ductile damage evolution law did manifest as expected. The resultant failure mode of the experimental test and numerical model of the circular pin is presented in the Figure 11.

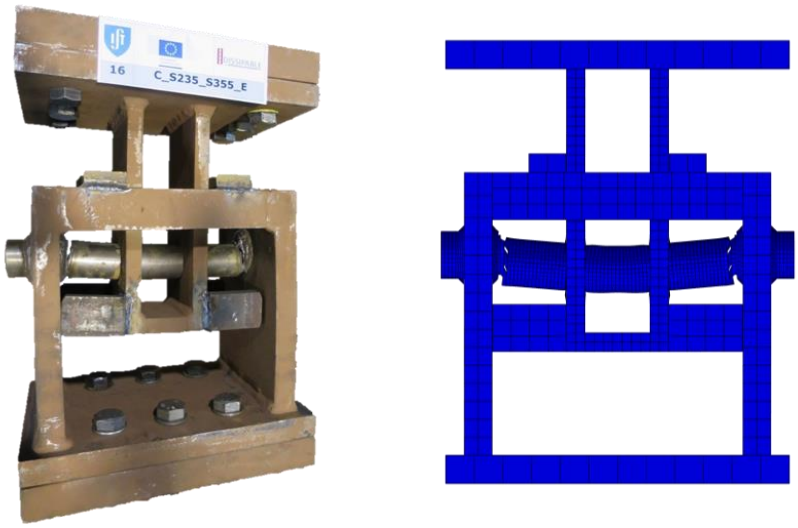

(a) (b)

Figure 11: Failure mode of circular pin section device: (a) experimental test, (b) numerical model

The shear failure mode near the interior welded sections obtained in the numerical model was very similar to what was observed at the end of the experimental test.

6. Conclusions

The experimental tests were carried successfully and gathered much information regarding the local behaviour of the DRBrC pin device. A major improvement on the pin device configuration was implemented during the experimental tests phase, the guiding plates. The guiding plates showed many benefits and should be considered as an integral component of the DRBrC pin device.

Regarding the pin device performance evaluation, the best configuration is the chamfered pin section, with the application of both guiding plates. The pin device configurations with a circular section and welded sections, although resulting in remarkably higher dissipated energy values, showed an early brittle failure of the welds. In real life applications this could cause greater consequences, due to the sudden and more unpredictable response.

The numerical models developed adequately verified the results obtained experimentally. The combined hardening characterization could not be performed rigorously because no cyclic tensile tests were performed to characterize the cyclic behaviour of the steel materials. Nevertheless, the numerical models developed allowed for a more in-depth evaluation.

The ductile damage criteria developed showed to be a promising tool and should be further investigated.

References

ABAQUS, 2012. Analysis User's Manual, Version 6.12. Dassault Systèmes, Providence, RI.

ECCS, 1986. Recommended Testing Procedure For Assessing the Behaviour of Structural Steel Elements under Cyclic Loads. Technical Committee 1 - Structural Safety and Loadings Technical Working Group 1.3 - Seismic Design N" 45, 0–11.

Myers, A.T., Deierlein, G.G., Kanvinde, A., 2009. Testing and probabilistic simulation of ductile fracture initiation in structural steel components and weldments. Report No. 170 333–350.

Plumier, A., Doneux, C., Castiglioni, C., Brescianini, J., Crespi, A., Dell'Anna, S., Lazzarotto, L., Calado, L., Ferreira, J., Feligioni, S., Bursi, O., Ferrario, F., Sommavilla, M., Vayas, I., Thanopoulos, P., Demarco, T., 2004. Two innovations for earthquake-resistant design: the INERD project. Luxembourg: European Comission, Research Fund for Coal and Steel 75–130.

Vayas, I., Thanopoulos, P., Tsarpalis, P., Dimakogianni, D., Henriques, J., Degee, H., Hoffmeister, B., Pinkawa, M., Castiglioni, C.A., Alavi, A., Brambilla, G., Calado, L., Proença, J.M., Sio, J., Chesoan, A., Stratan, A., Dubina, D., Neagu, C., Dinu, F., Georgiev, T., Raycheva, L., Zhelev, D., Rangelov, N., Morelli, F., Natali, A., Salvatore, W., Butz, C., Renzi, V., Butz, C., Medeot, R., 2017. Innovative Anti-Seismic Devices and Systems (INNOSEIS), 1st ed. ECCS - European Convention for Constructional Steelwork.